IL NUOVO CIMENTO **43 C** (2020) 113
DOI 10.1393/ncc/i2020-20113-5

COMMUNICATIONS: SIF Congress 2019

Transition-metal dichalcogenides with type-II Dirac fermions: Surface properties and application capabilities

G. D'OLIMPIO

Department of Physical and Chemical Sciences - L'Aquila, Italy

received 31 January 2020

Summary. — Among the various layered materials "beyond graphene", the class of transition-metal dichalcogenides MTe_2 (M= Ni, Pd, Pt) is particularly interesting, due to the existence of bulk type-II Dirac fermions, arising from a tilted Dirac cone. The Dirac cone in these materials is located in the bulk, with inherently superior robustness to surface modifications compared to other Dirac materials, among which graphene, topological insulator and silicene. In addition, MTe_2 also displays application capabilities in optoelectronics and catalysis. Here, with surface-science experiments and theory, we assess the surface properties of MTe_2, including i) ambient stability, ii) chemical reactivity and iii) aging mechanisms. Remarkably, MTe_2 shows outstanding tolerance to CO and stability in water environment. We also demonstrate that passivation in ambient atmosphere is achieved in less than 30 minutes with the TeO_2 skin having a sub-nanometric thickness even after one year in the air. The existence of Te vacancies leads to the enhancement of the surface chemical reactivity. These results pave the way toward the exploitation of this class of Dirac materials in optoelectronics and catalysis.

1. – Introduction

In recent years, transition-metal dichalcogenides (TMDCs) have been attracting considerable attention for their application capabilities in optoelectronics [1-3], catalysis [4,5], gas separation [6] and desalination [7]. Especially, the interest toward a specific class of TMDCs constituted by $NiTe_2$, $PdTe_2$ and $PtTe_2$ is further motivated by the existence of bulk type-II Dirac fermions, arising from a tilted Dirac cone [8]. Recently, type-II Dirac fermions have been experimentally observed in $PtTe_2$ [9,10], $PdTe_2$ [11,12] and $NiTe_2$ [13]. To take advantage of their extraordinary technological potential, the assessment of their chemical and thermal stability is crucial [14]. Definitely, ambient instability is associated to the chemical reactivity of the surface [15] and to the presence of defects [16]. To scale up the fabrication of nanodevices, ambient stability is particularly crucial in order to prevent the use of a capping layer on the active channel.

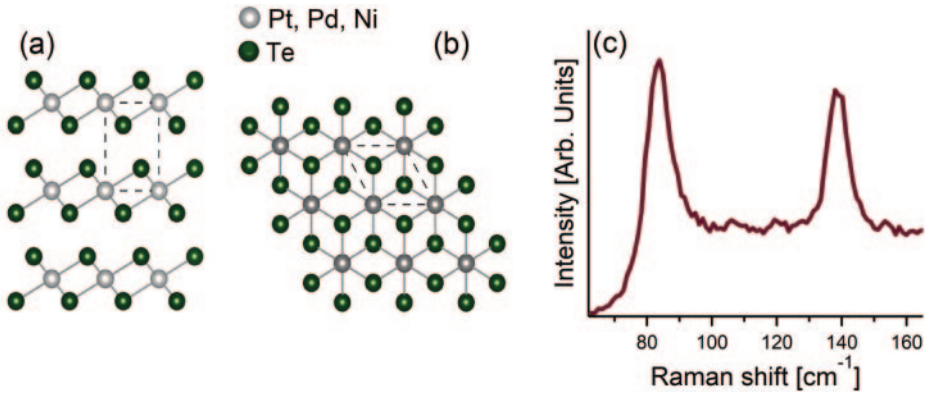

Fig. 1. – (a) Side and (b) top views of the atomic structure of Pt, Pd, $NiTe_2$. Grey balls denote Pt, Pd or Ni atoms, while green balls represent Te atoms. (c) Raman spectrum of $NiTe_2$ single crystal acquired at room temperature with laser $\lambda = 632.8\,\text{nm}$.

Usually, the surface termination of TMDCs is constituted by an atomic layer of chalcogens [17]. The critical role in surface stability is due to the lone pair electrons of chalcogen atoms [18]. Therefore, minimizing the amount of chalcogen vacancies is important for surface protection from unwanted reactions with environmental species, especially surface oxidation [17, 19-21].

Herein, we have studied the electronic properties and, moreover, the chemical and thermal stability of these materials through density functional theory (DFT) and experiments by X-ray photoelectron spectroscopy (XPS) and high-resolution electron energy loss spectroscopy (HREELS). We show that the Te termination in an oxygen-rich environment (as in ambient atmosphere) evolves in a sub-nanometric passivation layer of TeO_2, which saturates in a few minutes and remains stable in a timescale extended up to one year. The formation of tellurium-oxide phases is favored in the presence of Te vacancies. Moreover, $PtTe_2$, $PdTe_2$ and $NiTe_2$ also represent good candidates for perfectly CO-tolerant electrodes for electrocatalysis [22, 23].

These materials crystallize in the CdI_2-type trigonal (1T) structure with P-3m1 space group (No. 164), sketched in fig. 1, panels (a) and (b). Each transition metal atom at the basal plane is surrounded by six Te atoms, forming Ni(Pd,Te)Te_6 octahedra. The bulk $NiTe_2$ single crystal shows two Raman active modes at around 84 and 138 cm^{-1} (fig. 1(c)). These phonons modes can be assigned to E_g and A_{1g}.

2. – Experimental

2˙1. *Computational method and model.* – The atomic structure and energetics of various configurations of various gases adsorbed on $NiTe_2$ were studied by DFT using the QUANTUM-ESPRESSO code [24] and the GGA-PBE + van der Waals approximation, which is feasible for the description of adsorption of molecules on surfaces [25, 26]. We used energy cutoffs of 25 and 400 Ry for the plane-wave expansion of the wave functions and the charge density, respectively, and the $4 \times 4 \times 3$ Monkhorst-Pack k-point grid for the Brillouin zone sampling. For modelling the $NiTe_2$ surface, we used a slab of three layers. Physisorption enthalpies were calculated by the standard

formula:

$$\Delta H_{phys} = [E_{host+mol} - (E_{host} + E_{mol})],$$

where E_{host} is the total energy of the pristine surface, and E_{mol} is the energy of a single molecule of the selected species in an empty box. In the case of water adsorption, only the gaseous phase is considered. The chemisorption energy is defined as the difference between the total energy of the system with an adsorbed molecule and the total energy of the same system after decomposition of the same molecule on the surface. For the case of physisorption, we also evaluated the differential Gibbs free energy by the formula

$$\Delta G = \Delta H - T\Delta S,$$

where T is the temperature and ΔS is the change of entropy of the adsorbed molecule. The entropy was estimated considering the gas-to-liquid transition by the standard formula $\Delta S = \Delta H_{vaporization}/T$, where $\Delta H_{vaporization}$ is the measured enthalpy of vaporization.

2˙2. *Single-crystal growth.* – Single crystals of $NiTe_2$, $PdTe_2$ and $PtTe_2$ were grown using the Te flux method. The starting mixtures were made by Ni powder (99.99%) and Te ingots (99.9999%) in ratio 1:8 for $NiTe_2$, Pd sheet (99.9%) and Te powder (99.9999%) ratio 1:2 for $PdTe_2$ and Pt (99.99%) foil and Te ingot (99.9999%) in ratio of 1:17; each mixture were sealed under vacuum in a quartz tube. The flat surface of the crystal corresponds to the (001) plane. The crystal structure and phase purity of the as-grown crystals were identified by X-ray diffraction (XRD) (Bruker D2 PHASER) and Laue diffraction (Photonic Science) at room temperature.

2˙3. *Raman spectroscopy.* – Micro-Raman spectra were acquired at room temperature by using a LABRAM spectrometer with a 1800 lines/mm diffraction grating equipped with a He-Ne laser source ($\lambda = 632.8$ nm) and an optical microscope with a 100× MPLAN with numerical aperture of 0.9. The laser spot cross-diameter is $\sim 2\,\mu$m. The system operates in a back-scattering configuration.

2˙4. *AFM.* – AFM images were acquired with a Digital D5000, Veeco system operating in Tapping mode. The resonance frequency of the tip is 75 kHz.

2˙5. *HREELS.* – Vibrational experiments were carried out at room temperature with a Delta 0.5 spectrometer (Specs GmbH, Germany). The experimental resolution is 3–4 meV. Gases were dosed with precision leak valves.

2˙6. *Synchrotron radiation spectroscopies.* – XPS measurements were carried out on the CNR BACH beamline at Elettra Sincrotrone in Trieste (Italy) for $NiTe_2$ and at the High-Energy branch of the Advanced Photoelectric Experiments beamline (APE-HE) of the Elettra Synchrotron, Trieste, Italy for $PdTe_2$ and $PtTe_2$. Under our experimental conditions, we had any evidence of beam-induced damage even after long-time exposure to synchrotron light.

3. – Results and discussion

3˙1. *Electronic properties.* – In fig. 2, we provide a comparison of band structures of MTe_2 (with M = Ni, Pd, Pt). In group-X Pd- and Pt-based dichalcogenides, the bulk

Dirac node lies deep below the Fermi level (∼0.6, ∼0.8 and ∼1.2 eV in $PdTe_2$, $PtTe_2$, and $PtSe_2$, respectively) [9, 12], hindering their successful exploitation in technology. In contrast, $NiTe_2$ hosts low-energy type-II Dirac fermions [27]. Precisely, a pair of type-II Dirac nodes is present in $NiTe_2$ along the C_3 rotation axis, lying in the nearness of the Fermi energy (+20 meV), whose precise position can be easily manipulated by doping directly during the single-crystal growth in order to have the Dirac point below or above the Fermi level. Therefore, $NiTe_2$ is particularly suitable for exploration of Dirac fermiology and applications in TMDC-based spintronic devices and ultrafast optoelectronics.

3˙2. *Surface chemical reactivity*. – To evaluate the stability and the chemical reactivity of $NiTe_2$, $PdTe_2$ and $PtTe_2$, we modelled the energetics of the adsorption and decomposition of various gases on their surfaces (see table I).

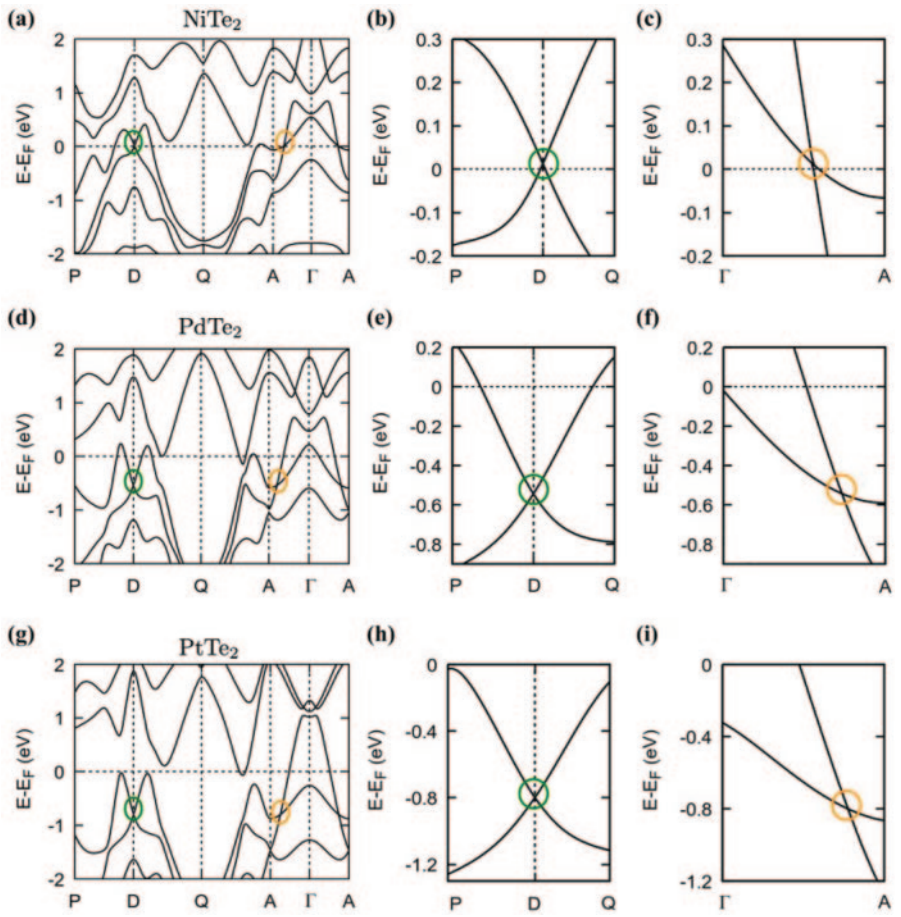

Fig. 2. – The band structure of $NiTe_2$, $PdTe_2$, and $PtTe_2$, showing the two Dirac points tilted in opposite directions, located on the A-Γ-A′ axis. The dispersion around each of the Dirac points is isotropic in the horizontal P-D-Q plane (parallel to the experimental Γ-K-M plane) and anisotropic and "tilted" along the Γ-A direction. A magnification of the band structure around one of the Dirac points, is shown in panels (b), (e) and (h) for the isotropic P-D-Q direction (marked by the green circle in (e)), and along the Γ-A′ direction in (X).

For $NiTe_2$ and $PdTe_2$ the differential Gibbs free energy ΔG for adsorption of molecular oxygen at room temperature is negative (-43.4 and -55.49 kJ/mol, respectively), thus indicating that its adsorption is energetically favorable. Decomposition of the adsorbed O_2 molecules is favorable for the case of oxygen for both $NiTe_2$ and $PdTe_2$ (-112.3 and -94.4 kJ/mol, respectively). Concerning water adsorption, it is energetically unfavorable at room temperature for both surfaces, as indicated by the positive values of ΔG $+3.1$ and $+11.9$ kJ/mol, respectively.

Conversely, adsorption of O_2 and H_2O on $PtTe_2$ is energetically unfeasible at room temperature, as the differential Gibbs free energy of adsorption is positive ($+46.3$ and $+1.8$ kJ/mol).

It is also particularly relevant to assess the energetics for CO chemisorption. As a matter of fact, Pt- and Ni-based alloys are usually affected by the problem of CO poisoning at room temperature [23, 28]. Moreover, the absorption of carbon monoxide is energetically unfavorable for both $NiTe_2$ and $PdTe_2$, with ΔG values of $+4.9$ kJ/mol and $+9.45$ kJ/mol, respectively. Thus, $NiTe_2$ and $PdTe_2$ are not affected by CO poisoning, thus suggesting their potential use as electrode materials for electrocatalysis [22, 23].

The impact of Te vacancies on surface chemical reactivity has been also assessed.

TABLE I. – *Differential enthalpy ΔH and differential Gibbs free energy ΔG of adsorption of CO, H_2O and O_2 at room temperature on pristine $NiTe_2$, $PdTe_2$, $PtTe_2$, $NiTe_{1.88}$, $PdTe_{1.88}$ and $PtTe_{1.88}$ surfaces, respectively and their related decomposition energy.*

Surface	Chemical species	Physisorption		Decomposition
		ΔH [kJ/mol]	ΔG [kJ/mol]	ΔH [kJ/mol]
$NiTe_2$	CO	-14.4	$+4.9$	–
	O_2	-54.6	-43.3	-112.3
	H_2O	-28.8	$+3.1$	$+169.9$
$NiTe_{1.88}$	CO	-85.9	-66.3	–
	O_2	-117.4	-106.1	$+9.7$
	H_2O	-15.0	$+16.3$	$+151.7$
$PdTe_2$	CO	-9.9	$+9.4$	–
	O_2	-66.7	-55.4	-94.4
	H_2O	-19.3	$+11.9$	$+131.4$
$PdTe_{1.88}$	CO	-9.4	$+9.9$	–
	O_2	-53.7	-52.4	-92.2
	H_2O	-20.2	$+11.0$	$+167.6$
$PtTe_2$	O_2	-9.5	$+1.8$	$+224.4$
	H_2O	$+15.0$	$+46.3$	$+153.7$
$PtTe_{1.88}$	O_2	-223.4	-212.1	-215.6
	H_2O	-207.2	-175.9	$+156.6$

In particular, the adsorption of molecular oxygen becomes favorable for $PtTe_{1.88}$ and $NiTe_{1.88}$ ($\Delta G = -212.1$ kJ/mol, $\Delta G = -106.1$ kJ/mol) with respect to the pristine surfaces of $PtTe_2$ and $NiTe_2$, while no substantial changes between $PdTe_{1.88}$ and $PdTe_2$ exist. Conversely, when implanting Te vacancies in $PtTe_2$, adsorption of O_2 and H_2O becomes particularly favorable at Te-vacancies sites ($\Delta G = -212.1$ and -175.9 kJ/mol)).

The decomposition of oxygen is favorable for $PtTe_2$ and $PdTe_2$ ($\Delta H = -215.6$ and -94.4 kJ/mol), while for $NiTe_2$ it is energetically unfeasible ($\Delta H = +9.7$ kJ/mol). Notably, water splitting is energetically unfavorable on all surfaces.

To validate the theoretical results, we carried out experiments using several surface-science techniques. Each of these probes a different property of the material, so that the combination of tools provides a comprehensive understanding of the surface physic-ochemical properties.

To assess the surface chemical reactivity of $NiTe_2$, $PdTe_2$ and $PtTe_2$, we performed high-resolution X-ray photoelectron spectroscopy (XPS) experiments (figs. 3 and 4).

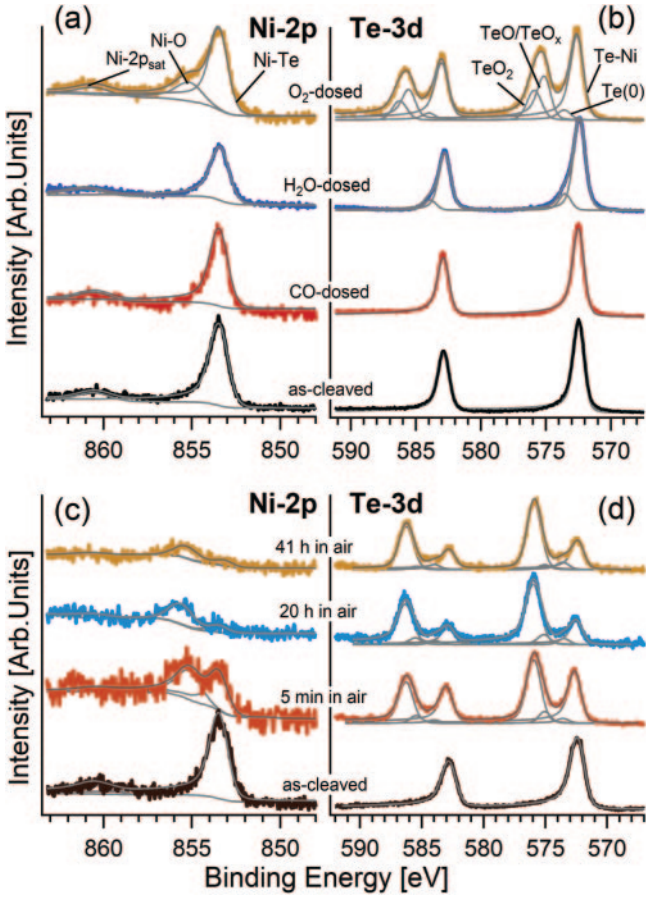

Fig. 3. – Core-level spectra of (a) Ni-2p and (b) Te-3d for as-cleaved $NiTe_2$ and for the same surface exposed to CO, H_2O and O_2 at $2 \cdot 10^4$ L, respectively. Core-level spectra of (c) Ni-2p and (d) Te-3d for as-cleaved $NiTe_2$, 5 min in air, 20 h in air and 41 h in air on $NiTe_2$, respectively. The photon energy is 1000 eV and the spectra are normalized to the maximum.

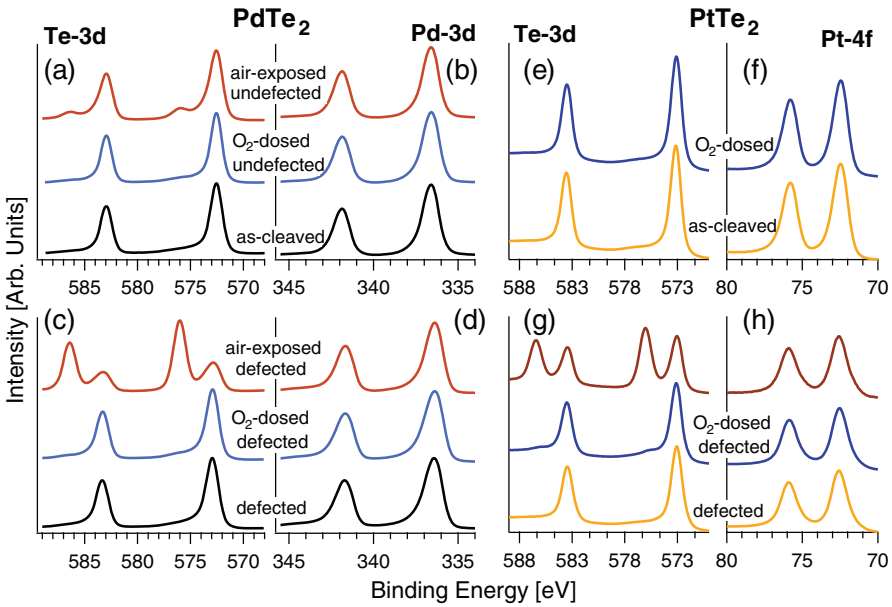

Fig. 4. – (a), (b) Te-3d and Pd-3d core levels for pristine, as-cleaved surface of $PdTe_2$ and for its modification upon O_2 dosage (10^5 L) and air exposure. Panels (c), (d) report the same for defected ($PdTe_{1.7}$). (e), (f) Pt-4f and Te-3d core levels taken for pristine $PtTe_2$ sample and the same surface exposed to 10^6 L of O_2. (g), (h) defected $PtTe_{1.6}$, the same surface exposed to 10^6 L of O_2 and air exposure. The photon energy is 800 eV and the spectra are normalized to the maximum.

We focused on the evolution of core levels upon various treatments. In figs. 3(a), (b) we show the Ni-2p and Te-3d core level for the as-cleaved $NiTe_2$ and the same surface after the exposure toward different gases. The Ni-2p core levels are practically unchanged upon CO dosage. Similarly, H_2O exposure just attenuates the signal by 60% but without the emergence of novel features, thus excluding any water adsorption at Ni sites. No changes in the Te-3d spectrum after CO exposure. Conversely, a new component at 573.4 eV, ascribed to the formation of the Te(0) species [29], appears in the Te-3d spectra after H_2O exposure.

From the analysis of XPS spectra in figs. 4(a)–(b), we infer that the as-cleaved undefected surfaces of $PdTe_2$ and $PtTe_2$ are inert toward oxygen exposure up to 10^6 L ($1\,\mathrm{L} = 1.33 \times 10^{-6}\,\mathrm{Torr} \cdot \mathrm{s}$). In fact, the Te-3d core level is unchanged for $PdTe_2$ and $PtTe_2$ (figs. 4(a), (b) and (e), (f), respectively) [17]. In defected surfaces, some changes occur in the case of $PtTe_{1.88}$, where from figs. 4(c), (g) we can note the emergence of the TeO_2 component [30, 31].

Different behaviour is found in O_2-dosed $NiTe_2$. The intensity of the Ni-2p level is reduced by 42% with the emergence of a new component at 855.5 eV (BE), which is related to Ni-O bonds [32]. Correspondingly, new components of Te-3d appear at higher BEs. The appearance of novel components located at 576.0 and 575.1 eV can be ascribed to the formation of TeO_2 and TeO_x [29-31]. The effects of CO, O_2 and H_2O gas exposure on the electronic properties of $NiTe_2$ were also assessed by measuring valence-band spectra (fig. 5(a)). The consistency of these spectra demonstrates that the electronic properties are negligibly affected by gas exposure.

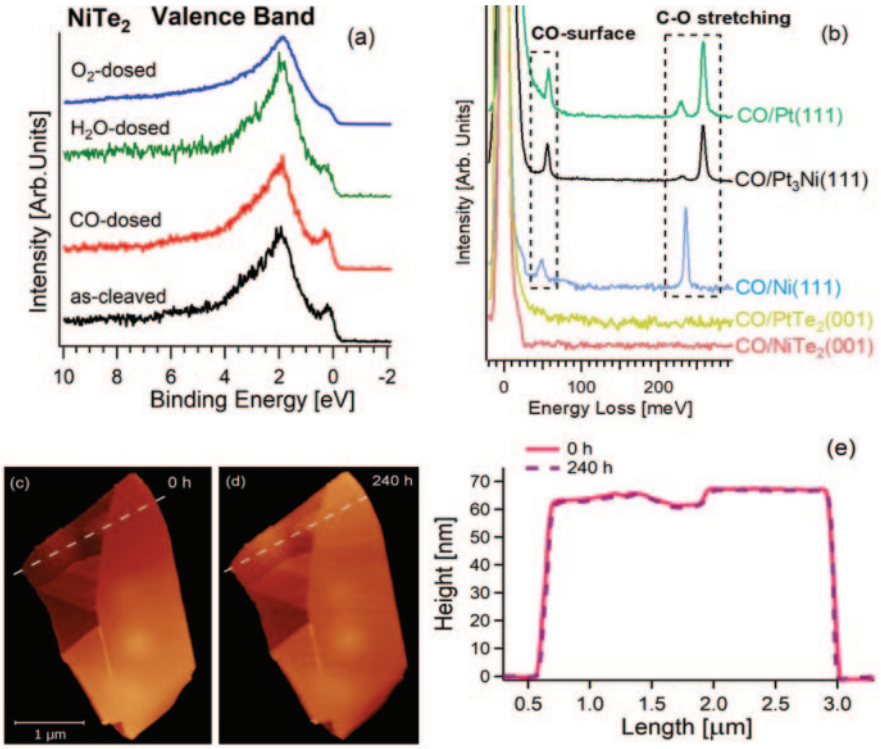

Fig. 5. – (a) Valence band for as-cleaved $NiTe_2$ and for the same surface exposed to CO, H_2O and O_2, respectively. The photon energy is 596 eV and the spectra are normalized to the maximum. (b) Vibrational spectra after having saturated with CO the surfaces of $NiTe_2(001)$, $PtTe_2(001)$, Ni(111), $Pt_3Ni(111)$ and Pt(111). The saturation has been reached at only 5, 10, and 8 L (1 L = 10^{-6} Torr · s) for Ni(111), $Pt_3Ni(111)$ and Pt(111). On the other hand, no CO-derived features are achieved even after exposure to 10^{10} L on $NiTe_2(001)$ and $PtTe_2(001)$. Specifically, the CO-derived features are the vibration of the whole CO molecule against the substrate at 50 meV and the intramolecular C-O stretching, whose energy depends on the adsorption site: 230 meV for three-fold site, selectively occupied on Ni [36], while it is minoritary on $Pt_3Ni(111)$ [28, 37] and Pt(111) [28], and 250 meV for the on-top adsorption site, majoritary on both $Pt_3Ni(111)$ and Pt(111). (c), (d) Time evolution of AFM images of a 70 nm thick flake of $NiTe_2$. Panel (c) shows the flake immediately after exfoliation, while panel (d) shows the same flake after 240 hours in air. The dotted white lines indicate the path of the height profile shown in panel (e).

We directly assessed the problem by CO poisoning by exposing a $NiTe_2$ sample to CO by using the technique with highest sensitivity to CO adsorption, *i.e.*, high-resolution electron energy loss spectroscopy (HREELS), due to the high oscillating dipole for the C-O intramolecular stretching [33-35]. Specifically, we dosed CO to: i) $NiTe_2(001)$; ii) $PtTe_2(001)$; iii) Ni(111); iv) $Pt_3Ni(111)$; and v) Pt(111) surfaces, see fig. 5(b). Experiments were carried out in specular conditions to activate the dipole scattering regime. We obtain that, while Ni(111), $Pt_3Ni(111)$ and Pt(111) are poisoned by CO, as evidenced by the observation of C-O stretching and the CO-substrate vibrations, $NiTe_2$ and $PtTe_2$ are totally inert toward CO, even after prolonged CO exposure up to 10^{10} L.

3˙3. *Ambient stability.* – The as-cleaved $NiTe_2$, $PdTe_2$ and $PtTe_2$ were also directly exposed to the atmosphere with the aim to assess their ambient stability. As shown in

figs. 3(c), (d) and figs. 4(c), (d) and (g), (h) for the case-study example of $NiTe_2$, we studied the evolution of Te core levels as a function of exposure time in air. Definitely, a few minutes of exposure in air are sufficient to create a passivation layer of TeO_2, whose thickness is estimated to be $\sim$7 Å by quantitative XPS [38, 39]. A prolonged exposure time (up to 2 days) does not induce further oxidation of the $NiTe_2$ surface. Especially, the analysis of Te-3d core levels after 5 minutes in air indicates the formation of only a slight amount of Te(0) species, together with TeO_x and TeO_2 species. The TeO_x is converted in TeO_2 over the time, while Te(0) remains constant. The TeO_2 component reached the maximum after 30 min in air and no further changes emerge over the time. Correspondingly, the Ni-2p core level displays a NiO component that reaches a maximum after 30 minutes, and no further changes were observed for a longer time exposure. To evaluate the environmental stability, we also performed time-evolution atomic force microscopy (AFM) experiments on mechanically exfoliated flakes (figs. 5(c)–(e)). The evolution was followed on a timescale of up to 10 days. The AFM results demonstrate that exposure to the atmosphere does not change the morphology of the flakes, as confirmed by the height profile along a specific direction remaining constant with exposure (fig. 5(e)).

In the case of $PdTe_2$, we evaluated the thickness of the TeO_2 skin after air exposure to be $\sim$3 Å after 10 min and $\sim$9 Å after 1 year. With the aim to evaluate the impact of Te vacancies, we have repeated experiments for a sample with implanted Te vacancies ($PdTe_{1.7}$). However, any noticeable difference with the pristine, undefected sample is observed, except for a faster oxidation kinetics. Precisely, the TeO_2 skin is already $\sim$5.8 Å after 10 minutes in air.

Results on ambient stability shown in fig. 5 are consistent with the fabrication of microwave receivers with an active channel of uncapped $PdTe_2$ that showed minimal changes in the photosignal even after one week in air, as we showed elsewhere [40]. Therefore, the ambient stability of MTe_2 materials implies that capping layer can be avoided in the nanofabrication process of devices, in contrast with the cases of black phosphorus [41] and silicene [42].

4. – Conclusions

We have demonstrated that bulk $NiTe_2$, $PdTe_2$ and $NiTe_2$ are ambient-stable materials with type-II Dirac fermions. These materials are stable in air, except for the formation of a sub-nanometric TeO_2 skin in surfaces exposed to air. Passivation is reached in less than 30 minutes and no substantial changes are observed even after air exposure in a timescale extended up to one year. Their surfaces are inert toward H_2O and CO, enabling the possibility to fabricate CO-tolerant electrodes for electrocatalysis that would be stable in an aqueous environment. We have also highlighed the impact of Te vacancies on surface oxidation. Therefore, the growth of high-quality single crystals with minimized Te vacancies is crucial to favor the technological exploitation of this novel class of transition-metal dichalcogenide hosting type-II Dirac fermions. These results are important in devising applications in the fields of catalysis and nanoelectronics.

* * *

The author acknowledges P. Torelli, S. Nappini and F. Bondino for the XPS measurements; D. Boukhvalov, A. Agarwal and B. Ghosh for the computational model.

REFERENCES

[1] Zongliang G. *et al.*, *Appl. Phys. Lett.*, **114** (2019) 153102.
[2] Zeng L.-H. *et al.*, *Adv. Funct. Mater.*, **29** (2019) 1806878.
[3] Huang Xu *et al.*, *Small*, **15** (2019) 1903362.
[4] Zhuang P. *et al.*, *Adv. Funct. Mater.*, **29** (2019) 1901290.
[5] Chia X. and Pumera M., *Chem. Soc. Rev.*, **47** (2018) 5602.
[6] Shen J. *et al.*, *Adv. Funct. Mater.*, **28** (2018) 1801511.
[7] Li W. *et al.*, *ACS Nano*, **10** (2016) 1829.
[8] Soluyanov A. *et al.*, *Nature*, **527** (2015) 495.
[9] Yan M. *et al.*, *Nat. Commun.*, **8** (2017) 257.
[10] Politano A. *et al.*, *Phys. Rev. Lett.*, **121** (2018) 086804.
[11] Noh H.-J. *et al.*, *Phys. Rev. Lett.*, **119** (2017) 016401.
[12] Clerk O. J. *et al.*, *Phys. Rev. Lett.*, **120** (2018) 156401.
[13] Xu C. *et al.*, *Chem. Mater.*, **30** (2018) 4823.
[14] Thakur R. *et al.*, *Nanoscale*, **11** (2019) 10716.
[15] Politano A. *et al.*, *FlatChem*, **1** (2017) 60.
[16] Zhou W. *et al.*, *Nano Lett.*, **13** (2013) 2615.
[17] Politano A. *et al.*, *Adv. Funct. Mater.*, **28** (2018) 1706504.
[18] Chhowalla M. *et al.*, *Nat. Chem.*, **5** (2013) 263.
[19] Qirong Y. *et al.*, *J. Phys. Chem. C*, **122** (2018) 25498.
[20] Soumya Ranjan D. *et al.*, *J. Phys. Chem. C*, **122** (2018) 17001.
[21] Afanasiev F. and Lorentz c., *J. Phys. Chem. C*, **123** (2019) 7486.
[22] Li Q. *et al.*, *J. Electrochem. Soc.*, **150** (2003) A1599.
[23] Politano A. and Chaiarello G., *J. Phys. Chem. C.*, **115** (2011) 13541.
[24] Giannozzi P. *et al.*, *J. Phys. Condens. Mater.*, **21** (2009) 395502.
[25] Perdew J. P., Burke K. and Ernzerhof M., *Phys. Rev. Lett.*, **77** (1996) 3865.
[26] Barone V. *et al.*, *J. Comput. Chem.*, **30** (2009) 934.
[27] Ghosh B. *et al.*, *Phys. Rev. B*, **100** (2019) 195134.
[28] Chiarello G. *et al.*, *J. Chem. Phys.*, **134** (2011) 224705.
[29] Bahl M. K. *et al.*, *J. Chem. Phys.*, **66** (1977) 5526.
[30] Berchenko N. *et al.*, *Appl. Surf. Sci.*, **452** (2018) 134.
[31] Galco A. C. *et al.*, *J. Non-Cryst. Solids*, **499** (2018) 1.
[32] Meeporn K., Chanlek N. and Thongbai P., *RSC Adv.*, **6** (2016) 91377.
[33] Bartons B. *et al.*, *Surf. Sci.*, **179** (1987) 59.
[34] Baro A. M. and Ibach H., *J. Chem. Phys.*, **71** (1979) 4812.
[35] Jacobi K. *et al.*, *J. Electron. Spectrosc.*, **54-55** (1990) 529.
[36] Politano A., Formoso V. and Chiarello G., *Surf. Sci.*, **602** (2008) 2096.
[37] Politano A. and Chiarello G., *RSC Adv.*, **4** (2014) 45641.
[38] Alexander M. R. *et al.*, *Surf. Interface Anal.*, **34** (2002) 485.
[39] Sciortino L. *et al.*, *Surface investigation and aluminum oxide estimation on test filters for the ATHENA X-IFU and WFI detectors*, in *Proceedings of SPIE*, Vol. **9905** (International Society for Optics and Photonics) 2016.
[40] D'Olimpia G. *et al.*, *Adv. Funct. Mater.*, **30** (2020) 1906556.
[41] Island J. *et al.*, *2D Mater.*, **2** (2015) 011002.
[42] Wang R. *et al.*, *Sci. Rep.*, **3** (2013) 3507.